Modeling atmospheric circulations with soundproof equations

Piotr K. Smolarkiewicz

National Center for Atmospheric Research
Boulder, Colorado, U.S.A.
smolar@ucar.edu

ABSTRACT

Advances are discussed in the area of nonhydrostatic soundproof equations. The performance of the governing soundproof partial differential equations for scales relevant to climate and weather is highlighted with global aquaplanet and baroclinic instability calculations using a research model EULAG (www.eulag.org). Consistent numerical integrals of the anelastic Lipps-Hemler and the pseudo-incompressible Durran systems are compared with hydrostatic results. On the algorithmic side, a progress towards an unstructured-mesh option of EULAG is illustrated with simulations of atmospheric wave dynamics across a range of scales

1 Introduction

A lesson learned from the collection of works in the special issue [1] is that there is no set of governing equations uniformly adopted throughout the NWP community, and all operational models differ in some aspect already at the theoretical level. In spite of the ongoing debate on the preferred theoretical formulation of the governing partial differential equations (PDEs), the dominant opinion seems to be that soundproof equations are not appropriate for predicting weather and climate. On the other hand, the soundproof models progress, expand their predictive skill and range of validity, and keep attracting interests of the community. In particular, the last decade saw numerous developments consequential for the advancement of nonhydrostatic soundproof models for weather and climate. For substantiation, consider an abbreviated list of works exemplifying the community efforts. The list starts with [2] that quantified departures of normal modes of atmospheric soundproof PDEs from normal modes of the fully compressible Euler equations. Although the authors questioned the suitability of soundproof equations for weather and climate, their work in fact extended the validity of anelastic models beyond the earlier arguments of scale analyses [3, 4]. In [5, 6] soundproof models were generalized to incorporate time-dependent curvilinear coordinates, thereby enabling approximations of elastic boundaries (such as finite-amplitude free surface) in soundproof equations and facilitating a coupling of nonhydrostatic anelastic and hydrostatic primitive equation models; see [6] for examples. More recently, the work [8] generalized the pseudo-incompressible system [9] to spatially inhomogeneous and time-dependent reference states, extending up-scale the accuracy of soundproof approximations. Concomitantly, in [10, 11] the authors compared standard aquaplanet simulations [12, 13] conducted with three different dynamic cores, including nonhydrostatic anelastic model EULAG [14], within the framework of the Community Atmosphere Model (CAM). They reported favorable comparability of EULAG with the spectral and finite-volume hydrostatic dynamic cores, and found no evidence of inadequacy of anelastic nonhydrostatic equations for climate simulations, epitomized by the aquaplanet benchmark. In a recent work [15] the authors proposed a hybrid system of atmospheric PDEs combining nonhydrostatic soundproof and hydrostatic primitive equations, thus paving the road for a new class of general circulation models. Using techniques of multiple-scale asymptotic analysis, a current work [16] showed a formal validity of the Durran pseudo-incompressible [9] and the Lipps-Hemler anelastic [4] equations for realistic magnitudes of the tropospheric potential temperature stratification, in contrast to single-scale asymptotics [3] and

common beliefs. On the algorithmic side, the developments in [17, 18, 19] generalized proven conservative numerics of EULAG to fully unstructured meshes, while sustaining the accuracy of structured-grid differencing on differential manifolds. This adds yet another path to the advancement of soundproof models.

The goal of this paper is to address the performance of soundproof models in applications relevant to climate and weather, and to comment on the potential of unstructured meshes for meteorological simulation. Because all key results presented employ either EULAG or its derivatives, next section briefly summarizes the concepts behind this model. Section 3 brings to the reader's attention the results of [10] for the aquaplanet simulations using different dynamic cores in CAM, and supplements them with recent results [20] of the global baroclinic instability benchmark [21]. Section 4 highlights the progress with generalization of the class of nonoscillatory forward-in-time schemes that underlie the EULAG numerics on fully unstructured meshes. Remarks in section 5 conclude the paper.

2 EULAG, a numerical laboratory for atmospheric flows

The computational model EULAG is a general purpose virtual laboratory for simulating fluid flows across a wide range of scales and physical scenarios; see [14] for a review and a comprehensive list of references. Even though the primary applications are atmospheric circulations [22], the EULAG's optional dynamic cores encompass a range of diverse research areas, with extreme examples of micro flows in porous media [23] and global solar magnetohydrodynamics [24]. In consequence, the governing PDEs incorporate many options, including compressible/incompressible Boussinesq equations, fully incompressible (non Boussinesq) Navier-Stokes' equations, several anelastic systems including the Durran pseudo-incompressible equations [25], and fully compressible Euler equations of gas dynamics [17]. Furthermore, all the optional model PDEs are integrated with consistent numerical schemes, which is important for unobscured model intercomparisons.

The scope of this paper justifies a brief symbolic description of the governing soundproof equations. In general, to address a broad class of flows in a variety of domains — with, optionally, Dirichlet, Neumann, or periodic boundaries in each direction — the EULAG governing PDEs are formulated (and solved) in transformed time-dependent curvilinear coordinates [5, 6, 7]. Here, we dispense with geometric and numerical intricacies and refer the interested reader to technical expositions in the references provided. Furthermore, we focus attention on adiabatic, inviscid equations and numerical approximations using finite-volume conservative schemes. With these assumptions both the anelastic Lipps-Hemler and incompressible Boussinesq equations used in this paper can be technically viewed as special cases of the Durran pseudo-incompressible equations. The latter can be written in a perturbation form

$$\nabla \cdot (\rho^* \mathbf{v}) = 0 \; ; \quad \frac{D\theta'}{Dt} = -\mathbf{v} \cdot \nabla \theta_e \; ; \quad \frac{D\mathbf{v}}{Dt} = -\theta \nabla \pi' - \mathbf{g}\frac{\theta'}{\theta_e} - \mathbf{f} \times \left(\mathbf{v} - \frac{\theta}{\theta_e}\mathbf{v}_e \right) \; , \qquad (1)$$

where ρ^* denotes a generalized density, θ is potential temperature, vectors $\mathbf{g}$ and $\mathbf{f}$ are gravity acceleration and Coriolis parameter, π' is a normalized pressure-perturbation variable;[1] and primes symbolize deviations from geostrophically balanced environmental (ambient) state $(\mathbf{v}_e, \theta_e)$, implied by the governing equations. There are two noteworthy differences between the pseudo-incompressible system (1) and the Lipps-Hemler anelastic system. First, $\rho^* = \rho_b(\theta_b/\theta_o)$ in (1) but $\rho^* = \rho_b$ in the anelastic mass-continuity equation — subscript $_b$ refers to a static horizontally-homogeneous reference state, and θ_o denotes a constant reference value. Second, the momentum equation in (1) is non-approximated, whereupon factors proportional to θ appear in the pressure-gradient and Coriolis accelerations, and θ_e replaces θ_b in the denominator of the buoyancy term. Consequently, the differences between the pseudo-incompressible and anelastic solutions are expected to amplify with increasing stratification and/or with

---

[1]Note that the definition of the actual pressure variable in soundproof equations is flexible and depends on the coefficient in front of the gradient; cf. anelastic equations (5) in section 4.2.

increasing vertical and horizontal scales of the studied problem. Technically, the anelastic Lipps-Hemler equations reduce to the incompressible Boussinesq system by setting the reference profiles ρ_b and θ_b to constant values ρ_o and θ_o, respectively.

The prognostic equations in (1) are of the form $D\psi/Dt = R$, with ψ symbolizing either the potential temperature or a velocity component. Accordingly, their mathematically equivalent conservation-law form can be written as

$$\frac{\partial \rho^* \psi}{\partial t} + \nabla \cdot (\rho^* \mathbf{v} \psi) = \rho^* R \ . \tag{2}$$

The nonoscillatory forward-in-time algorithm employed in EULAG to integrate soundproof equations (2) to the second-order in time and space can be written in a compact functional form

$$\psi_i^{n+1} = \mathscr{A}_i(\tilde{\psi}, \mathbf{v}^{n+1/2}, \rho^*) + 0.5\delta t R_i^{n+1} \equiv \widehat{\psi}_i + 0.5\delta t R_i^{n+1}; \tag{3}$$

where ψ_i^{n+1} is the solution sought at the mesh point $(t^{n+1}, \mathbf{x}_i)$, $\tilde{\psi} \equiv \psi^n + 0.5\delta t R^n$, and $\mathscr{A}$ denotes a second-order-accurate finite-volume nonoscillatory two-time level transport scheme MPDATA [26, 27]. Equation (3) represents a system implicit with respect to all dependent variables in (1), because velocity, pressure, and potential temperature are assumed to be unknown at $n+1$. Due to nonlinearity of the pressure gradient term in (1), the algorithm (3) is executed iteratively

$$\theta'|_i^{n+1,\nu} = \widehat{\theta'}_i - 0.5\delta t \left(\mathbf{v}^{n+1,\nu} \cdot \nabla \theta_e\right)_i \tag{4}$$

$$\mathbf{v}_i^{n+1,\nu} = \widehat{\mathbf{v}}_i - 0.5\delta t \left[\theta^{n+1,\nu-1}\nabla \pi'|^{n+1,\nu} + \mathbf{g}\frac{\theta'|^{n+1,\nu}}{\theta_e} + \mathbf{f} \times \left(\mathbf{v}^{n+1,\nu} - \frac{\theta^{n+1,\nu-1}}{\theta_e}\mathbf{v}_e\right)\right]_i$$

where $\nu = 1, .., m$ numbers the iterations, and at each iteration the linear elliptic problem — implied by the continuity equation in (1) — is formulated on the mesh and solved using a preconditioned generalized conjugate-residual (GCR) approach; cf. [14] and references therein. Note that the only elements lagged behind in (4) are the $\propto \theta$ factors in the pressure-gradient and Coriolis accelerations. With the first guess $\theta^{n+1,0}$ predicted using the non-perturbation form of the entropy equation $D\theta/Dt = 0$ no iterations are required for second-order accuracy. Nonetheless, the iterations converge rapidly, add little overhead compared to the anelastic solver, and, in practice, there is no gain in using $m > 2$. For example in the global baroclinic instability calculations in the next section, $\| \theta'|^{n+1,\nu} - \theta'|^{n+1,\nu-1} \|_\infty \ \mathscr{O}(10^{-4})^\circ$K and $\mathscr{O}(10^{-6})^\circ$K for $m = 2$ and $m = 3$, respectively; while the work within the GCR solver decreases dramatically past $\nu = 1$. Furthermore, for solution of the anelastic and Boussinesq equations on a sphere an analogous iterative procedure is adopted to account for nonlinearity of the metric forces.

3 Soundproof models of idealized climate and weather

3.1 Aquaplanet simulations

For typical atmospheric conditions, the differences between the solutions of nonhydrostatic soundproof equations and either primitive hydrostatic equations or compressible Euler equations increase with the depth and horizontal extent of the simulated problem [2, 15]. Consequently, assessing the performance of the nonhydrostatic soundproof models in simulation of global weather and climate is mandatory. However, since there are no available operational NWP and climate codes based on nonhydrostatic soundproof equations, such assessments must start with idealized benchmarks. In the two part work [10, 11] the authors report on the implementation of EULAG, with the anelastic nonhydrostatic Lipps-Hemler governing PDEs, as a dynamical core in the Community Atmospheric Model (CAM, version 3). In particular, Part I [10] presents a series of aquaplanet simulations and demonstrates that CAM3-EULAG (CEU) results compare favorably with those from CAM simulations at standard CAM resolution that used current finite-volume (CFV) or Eulerian-spectral (CES) hydrostatic dynamical core
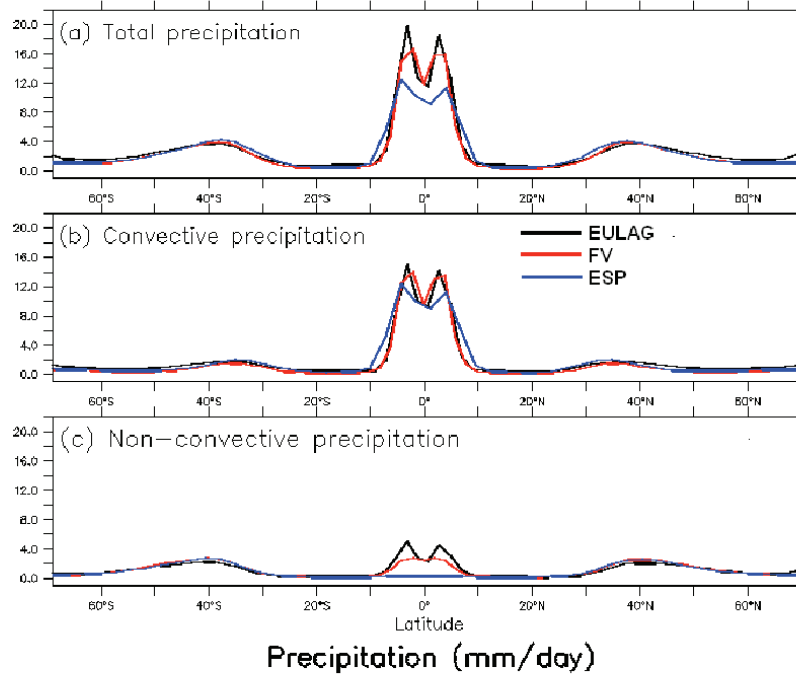
Figure 1: Zonally averaged total precipitation (mm day-1) from the aquaplanet simulations: a total precipitation, b convective precipitation, and c nonconvective precipitation.

options. In addition, both parts show the benefits of grid adaptivity implemented in CAM3-EULAG via generalized time-dependent curvilinear coordinates, allowing higher resolution in selected regions without evidence of anomalous behaviors anywhere in the model. For details of the model coupling, computational setups, and thorough solution analysis, the interested reader is referred to the original work. Here we only mention the key aspect of the experiment and highlight its outcome with a few selected results.

The model vertical domains extended to 50 mb in CFV and CES, and to 30 km in CEU; all resolved with 26 vertical levels. In the horizontal, the $2° \times 2.5°$ (meridional $\times$ zonal) resolution was used in CEU and CFV, and T42 in CES. Each experiment ran for 18 months of simulated time, with CEU initialized from rest and reaching statistical equilibrium after 4 months. Both CFV and CES were initialized from previous statistical steady states. The integration time step δt was 600 s in the CEU simulations and 900 s in the CFV and CES runs. All models were forced using a fixed zonally symmetric SST distribution — the same as the control case in [12] — with a maximum $27°C$ at the equator and a constant SST of $0\,°C$ poleward of $60°$ latitude in both hemispheres.

In general, the results in [10] evince quite similar dynamical fields for all three models, and CEU produces roughly the same climatology as CFV, CES and The Met Office Unified Model [13]. The basic features are sub-tropical westerly jets peaking at 12 km (190 mb) and $30°$ latitude in each hemisphere, and weak easterlies in the tropics and high latitudes (see their Fig. 4). CEU produces the weakest sub-tropical jets ($\sim$55 ms^{-1}) while CFV produces the strongest ($\sim$65 ms^{-1}). CES produces jets with the speed ($\sim$60 ms^{-1}), the same as in the [13] control simulation.[2] The tropical easterlies extend from the surface to 14-15 km ($\sim$150 mb) in CFV and CES, and extend from the surface to 13 km (190 mb) in CEU. The strongest easterlies below 4 km (600 mb) are about -10 ms^{-1} in all three models. The zonally averaged vertical winds from the models are also similar (see Fig. 5 in [10]) showing strong ascent in

---

[2]With an alternative CAM physics package, the CEU jets also reach the $\sim$60 ms^{-1} speed; Babatunde Abiodun, 2010, personal communication.

the tropics, subsidence in the sub-tropics, and a weak ascent in the mid-latitudes. The maxima of the tropical ascent are at 9-10 km (300 mb) and at $3°$ off-equator in both hemispheres. CEU simulates the strongest peaks (0.04 ms^{-1}), about twice the values in CES (0.018 ms^{-1}) and CFV (0.022 ms^{-1}). Below 800 mb CEU and CFV produce vertical winds of 0.012 ms^{-1}, twice the value in CES. This comparability, free of conclusive difference in favor of hydrostatic primitive equations, extends to thermodynamic fields of the potential temperature and moisture as well as to tropical convective activity. This is substantiated in Fig. 1 that shows zonally averaged rainfall. The three models produce maximum rainfall in the tropics and local maxima at mid-latitudes, and suppress precipitation in the sub-tropics and in high latitudes. The mid-latitude rainfalls from the models are in good agreement both in magnitude and location; all the models predict surface rainfall of about 4.0 mm day^{-1} at $38°$ latitude. In the tropics, CEU and CFV produce nearly the same precipitation, with a peak-to-peak average of $\sim$16 mm day^{-1}. CES produces a lower peak-to-peak average of $\sim$12 mm day^{-1}, consistent with CES's lack of non-convective precipitation in the tropics.
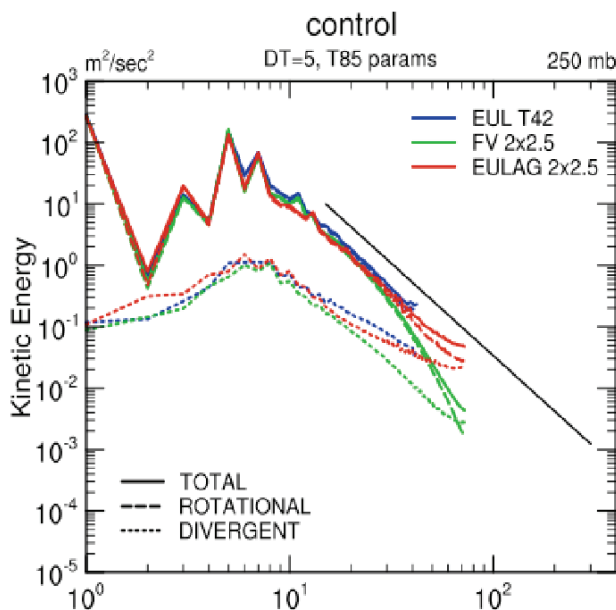

Figure 2: Kinetic energy spectra from the aquaplanet simulations; courtesy of David Williamson, NCAR.

To conclude, Fig. 2 shows kinetic energy spectra for the three models with common CAM physics package for the aquaplanet simulation. The figure is self-explanatory. Of particular note is an agreement with the planetary Rossby modes in terms of kinetic energy, notwithstanding the concerns expressed in [2].

3.2 Global baroclinic instability

The results of the preceding section addressed the performance of a soundproof model in archetypal climate simulations. One might argue that the demonstrated level of comparability of the nonhydrostatic anelastic and hydrostatic primitive-equations models owes much to filtering out in analyses many intermittent temporal and spatial scales important for weather prediction but possibly auxiliary to climate studies. Thus, to address the performance of soundproof models in meteorology simulations we consider here the global baroclinic instability benchmark [21] conducted with the Lipps-Hemler anelastic nonhydrostatic option of EULAG in [20]. We refer the interested reader to the latter work for the details of implementation, grid convergence study and a thorough discussion of the comparison with the hydrostatic primitive-equation results in [21]; here we only highlight a key conclusion of this study. Figure 3
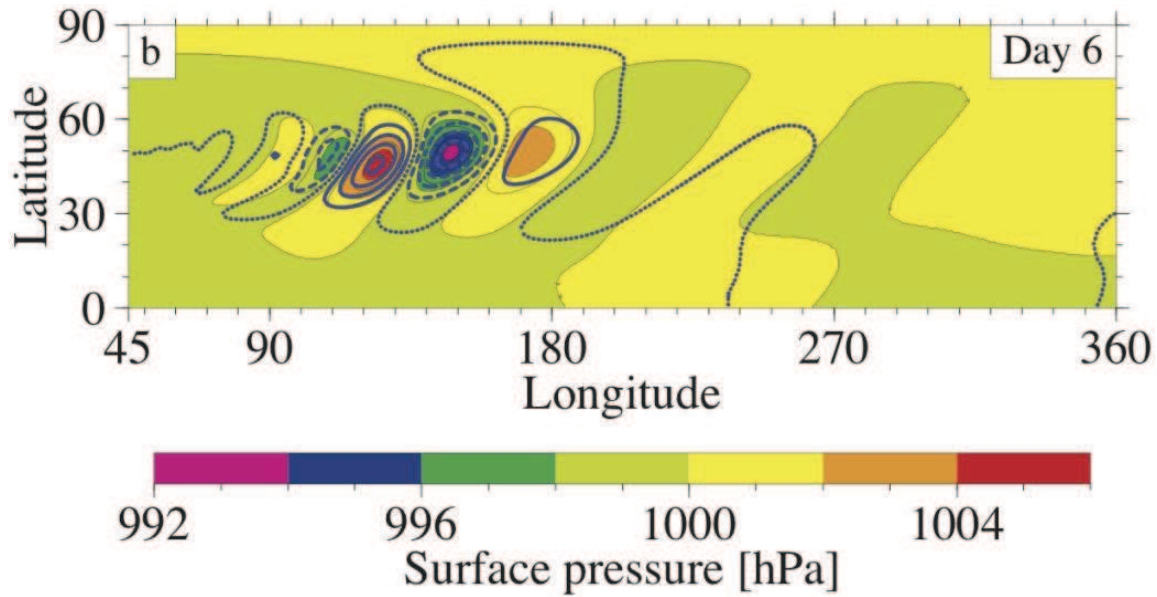
Figure 3: Baroclinic wave test, day 6 (linear phase of the evolution); surface pressures shown with color and lines correspond to the hydrostatic and anelastic results of [21] and [20], respectively.

compares surface pressures after 6 days of simulated evolution of the instability, a time representative of the linear growth phase. Noteworthy, the EULAG horizontal resolution $1.4°$ is twice coarser than that in [21], and the grid convergence study in [20] shows that the comparability of the wave group in the zonal improves for finer resolution. The result shown in Fig 3 reveals no pathologies predicted for the anelastic model in [2]. Furthermore, it illustrates a key conclusion in [20] that during the linear growth phase — the only time when phase speeds can be compared with high accuracy — differences between the EU-LAG and hydrostatic [21] dycore results are insignificant for the synoptic waves simulated here. During the baroclinic wavebreaking phase of the evolution, starting at about day 10 (not shown), differences between EULAG simulations and those of [21] emerge in details, while maintaining good agreement in the overall global structure of the flow. By 16 days, when the northern jet contains a broad range of scales, the two model solutions appear as two different realizations of a turbulent flow, with phases of various highs and lows advanced or retarded and amplitudes less or more accentuated in the two simulations. At this stage it is impossible to conclude which factors — differences in governing PDEs or model numerics — are responsible for the differences observed and which solution better captures the flow evolution.

In order to qualify the significance of comparability/disparity of the two model results in [20], Fig. 4 juxtaposes four solutions obtained with various EULAG options. All calculations used second-order numerics on a 64×128 ($2.8°$) lat-lon grid and 23 km deep domain resolved with 46 uniform $\delta z = 500$m grid intervals. The calculations in the left column of the figure employed the anelastic versus pseudo-incompressible PDEs, integrated with $\delta t = 300$ s by the same semi-implicit finite-volume scheme discussed in section 2. The calculations in the right column both employed the Lipps-Hemler anelastic equations but different numerical schemes. The result in the upper right panel used an explicit gravity-wave scheme with $D\theta/Dt = 0$ in lieu of the perturbation form in (1), whereas the one in the bottom panel used the default semi-implicit scheme but with the semi-Lagrangian (non-conservative) transport operator for $\mathscr{A}$ in (3); see [14] and the references therein for further discussion. Noteworthy, the explicit solution uses (and requires) 20 times smaller $\delta t = 15$s than semi-implicit runs. While the differences between the results in the two upper panel are minor, the explicit run is computationally about 20 times more expensive. In general, the differences between all three runs based on the Lipps-Hemler equations
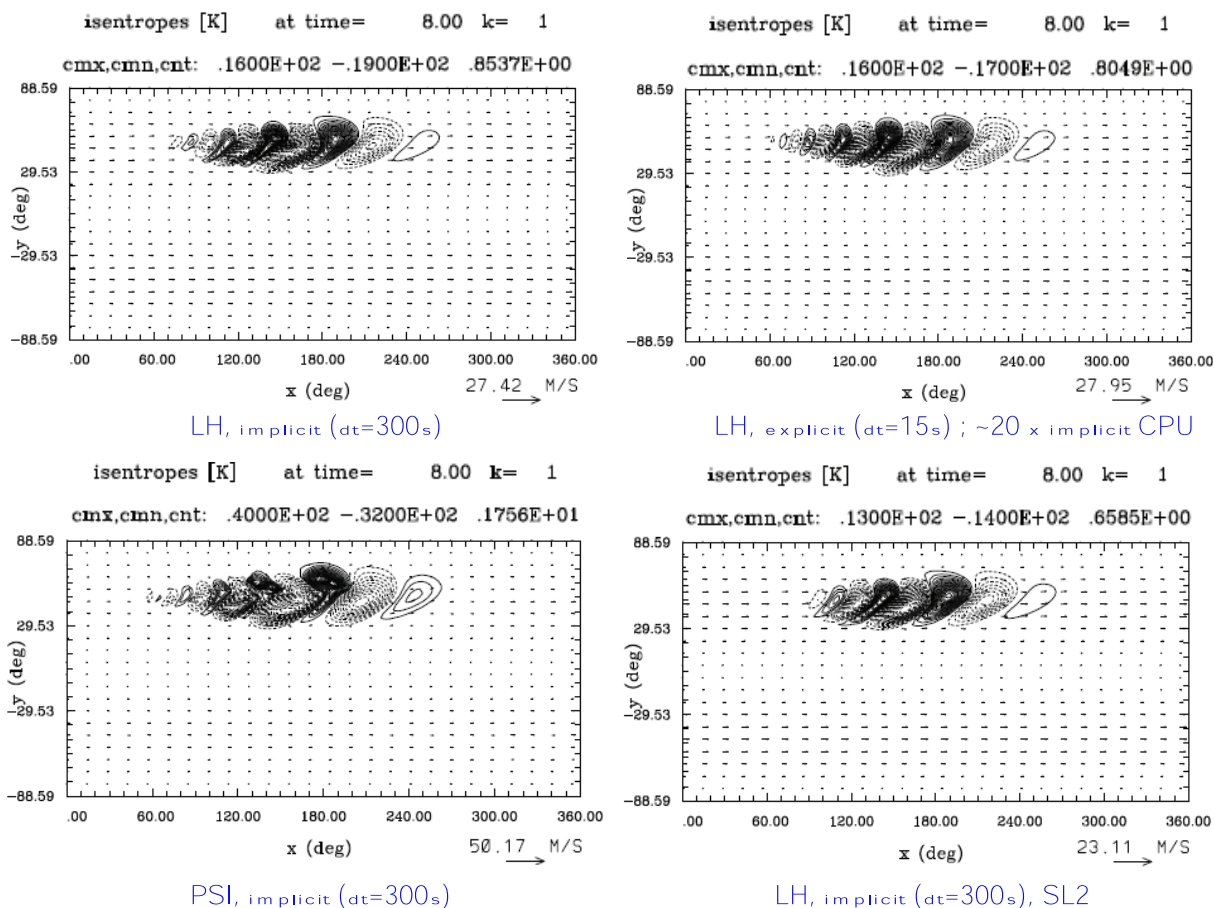
Figure 4: Baroclinic wave test, day 8, comparison of surface potential temperature perturbation using anelastic versus pseudo-incompressible EULAG options (upper and lower left, respectively) using the default semi-implicit finite-volume and a comparison of the anelastic option but using the explicit gravity-wave scheme versus semi-implicit but semi-Lagrangian integrator (upper and lower right, respectively).

are on the order of differences between the Lipps-Hemler and primitive hydrostatic equations discussed in [20]. Comparatively, the differences between the Lipps-Hemler and the Durran equations in the two panels on the left are dramatic. While the two solutions agree reasonably well phase wise, the pseudo-incompressible equations result in twice larger amplitude of the baroclinic wave. In terms of the wave amplitude, the evolution of the pseudo-incompressible solutions is about day ahead of the anelastic and hydrostatic solutions. An extensive sensitivity study aiming at better understanding of these solution behaviors is in progress, and its results will be reported elsewhere.

4 Unstructured mesh modeling of atmospheric waves

4.1 Background

The last decade saw increased interest and numerous developments in modeling atmospheric flows on meshes alternative to regular Cartesian grids common in meteorological models; see [28] for a substantiation. Although studies exploring unstructured meshing date back to the nineteen sixties [29], the interests in flexible mesh adpativity have emerged more recently (cf. the collection of papers in [30])

with the advent of multiscale Earth-system modeling and climate prediction. In spite of a high level of activity, as yet, adaptive-mesh atmospheric models have not met the demands of the modern operational weather prediction and climate studies, reviewed in the collection of works [1]. To date, research into unstructured mesh atmospheric models was largely confined to idealized applications addressing either synoptic flows in the lowest order long-wave approximation governed by the shallow water equations, or small-scale buoyant phenomena occurring in a neutrally stratified quiescent atmosphere — prototypes of natural convection and density currents. Compared to these two diverse classes of motions, applications addressing the dynamics of internal inertia-gravity waves are scarce. These waves are consequential for weather and climate and, because of their intricacy, numerical solutions of internal wave problems constitute canonical benchmarks for NWP codes. Here we highlight the progress with unstructured mesh modeling of atmospheric wave phenomena, following [17, 18, 19] and references therein.
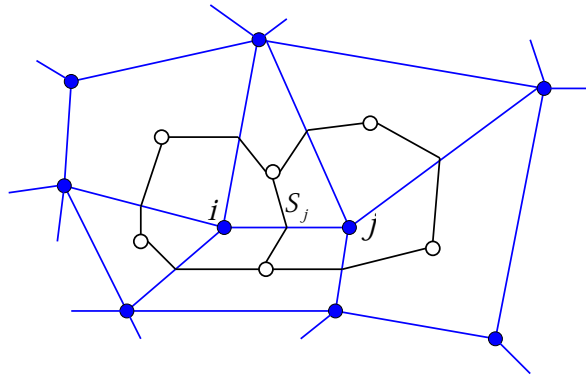

Figure 5: The edge-based, median-dual discretization approach in 2D. The edge connecting vertices (viz. data points) i and j pierces the face S_j shared by 2D computational (dual) cells surrounding vertices i and j. Open circles represent centers of the polygonal mesh cells; see [18] for a discussion.

The algorithmic framework suitable for the development of all-scale atmospheric flow unstructured/hybrid mesh models generalizes the methodologies proven in the structured grid model EULAG. A distinct key element of the framework is the suit of median-dual finite volume edge-based (Fig. 5; [31]) nonoscillatory advection schemes MPDATA, derived from first principles for an arbitrary unstructured mesh [27]. Remaining elements of the framework — a robust nonsymmetric Krylov-subspace elliptic solver [32] and a class of nonoscillatory forward-in-time (NFT) algorithms for integrating governing PDEs (see [17] for a recent review) — closely follow their structured grid predecessors. In EULAG the structured grid NFT framework is formulated in generalized time-dependent curvilinear coordinates, enabling dynamic grid adaptivity via continuous mappings in either Cartesian or spherical domains [14]. Unconventionally for flexible mesh models, the unstructured mesh NFT framework is also formulated in curvilinear coordinates. In particular, this is useful for modeling global circulations in spherical geometry [18] employing a classical geospherical reference frame with the governing equations cast in the latitude-longitude surface-based coordinates (section 7.2 in [33]). While retaining the benefits of the classical formulation, common in theoretical geo/astro physics, its notorious limitations associated with the convergence of meridians in the polar regions are circumvented by exploiting the flexibility of unstructured meshes. The latter is highlighted in Figure 6, which shows two alternate views of the mesh employed in simulations of global rotating stratified flows past an isolated mountain discussed in section 4.3.

4.2 A local area nonhydrostatic soundproof model

To illustrate the potential of unstructured meshes for meteorological simulation, here we highlight (after [19]) the performance of a local area nonhydrostatic soundproof model based on the governing PDEs
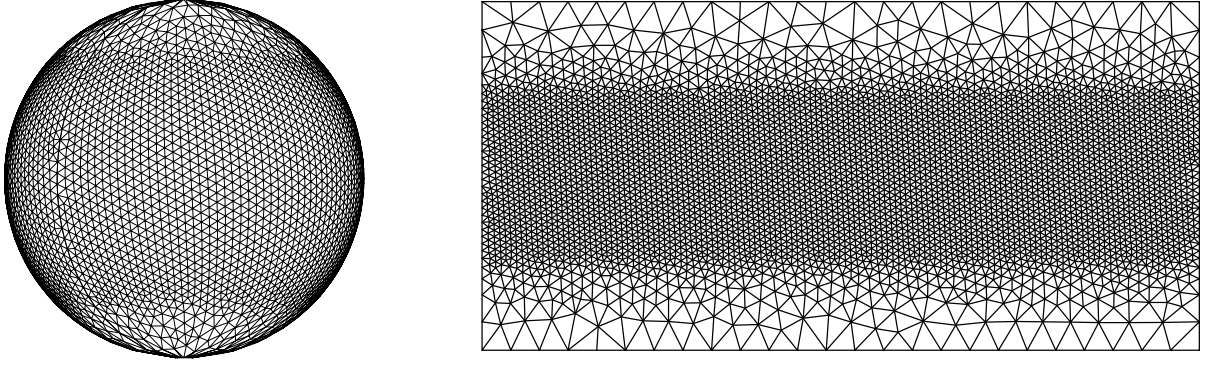
Figure 6: Triangular mesh in the physical space on a sphere and in a transformed (computational) latitude-longitude domain underlying the geospherical framework

written in the conservation-law form

$$\nabla \cdot (\rho_b \mathbf{V}) = 0 \,, \tag{5}$$
$$\frac{\partial \rho_b V^I}{\partial t} + \nabla \cdot (\rho_b \mathbf{V} V^I) = -\rho_b \frac{\partial \pi'}{\partial x^I} + \rho_b g \frac{\theta'}{\theta_o} \delta_{I3} \,,$$
$$\frac{\partial \rho_b \theta}{\partial t} + \nabla \cdot (\rho_b \mathbf{V} \theta) = 0 \,.$$

The system (5) is a special case of (1), and it encompasses several particular anelastic models depending on the selection of the reference profiles "$_b$". Here, V^I ($I = 1$ and $I = 3$) refers to the velocity components in the horizontal and the vertical, and $\pi' = (p - p_e)/\rho_b$ with p denoting the pressure. The Boussinesq benchmark problem addressed is a stratified ambient flow with a constant buoyancy frequency $N = 1\,\mathrm{s}^{-1}$ and uniform wind $\mathbf{V}_0 = (U_0, 0)$, $U_0 = 10\,\mathrm{ms}^{-1}$, impinging on an isolated ridge of the form $h(x) = h_0[1 + (x/L)^2]^{-1}$ centered at the origin of the $[-16.7L, 25L] \times [0, 25L]$ domain. The hill's half-width L is fixed, whereas the height $h_0 = 0.25L$ or $h_0 = 0.5L$. The respective Froude numbers, $Fr = U_0/Nh_0$, are $Fr = 1.66$ or $Fr = 0.83$ indicating a weakly- and strongly-nonlinear gravity-wave responses. The problem is nonhydrostatic, because $NL/U_0 = 2.4$; that is, the horizontal scale of the problem is comparable to the asymptotic wavelength $\lambda_0 \approx 2\pi U_0/N$ of the induced mountain wave.

Calculations were conducted on an unstructured mesh (Fig. 7; see also Fig. 2 in [19] for details) with approximately 39,500 vertices, refined to represent the hill geometry and the main portion of the wave train. The minimum spacing of vertices was prescribed at $L/12$ in the middle of the hill's base and was gradually reduced with altitude to $L/8$ spacing following the main wave train. The spacing was also smoothly reduced in the upwind and downwind directions (away from the main portion of the wave train) to $5L/3$ and $L/2$, respectively.

Figure 8 highlights the model solutions for the weakly- and strongly-nonlinear responses by showing the isentropes in a developing flow after dimensionless time $\tau = tU_0/L = 150$. In the former case, the mountain wave propagates at an angle $\alpha \approx 60°$ off the horizontal consistent with the linear steady-state theory prediction [19]. In contrast, for $Fr \lesssim 1$ the lee wave breaking and strong downslope winds (evidenced by isentrope compression) with the turbulent flow aloft are indicative of much studied wind-storm phenomena in mountainous terrain. Both solutions were compared with similar solutions generated with structured grid EULAG model, using the standard terrain-following mapping with a uniform spacing (in the computational space) of $\approx L/12$ covering identical domain with 157,184 grid points. Regardless of the fundamental differences in the spatial discretization the two model solutions match closely each other. For example, in the weakly-nonlinear case the structured grid and unstructured mesh solutions both differ from the linear theory estimates by no more than $\approx 3\%$ in the wavelength λ_0 and by no more
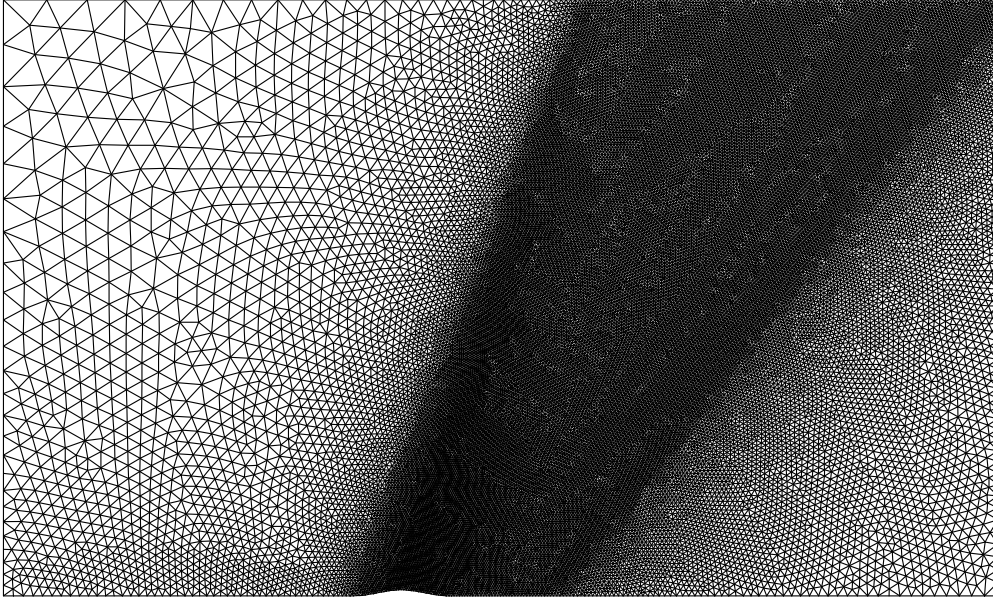
$$\nabla \bullet (\mathbf{V}\rho_o) = 0 \; ,$$

$$\frac{\partial \rho_o V^I}{\partial t} + \nabla \bullet (\mathbf{V}\rho_o V^I) = -\rho_o \frac{\partial \tilde{p}}{\partial x^I} + g\rho_o \frac{\theta'}{\theta_o}\delta_{I2}$$

$$\frac{\partial \rho_o \theta}{\partial t} + \nabla \bullet (\mathbf{V}\rho_o\theta) = 0 \; .$$

the refined triangular mesh.
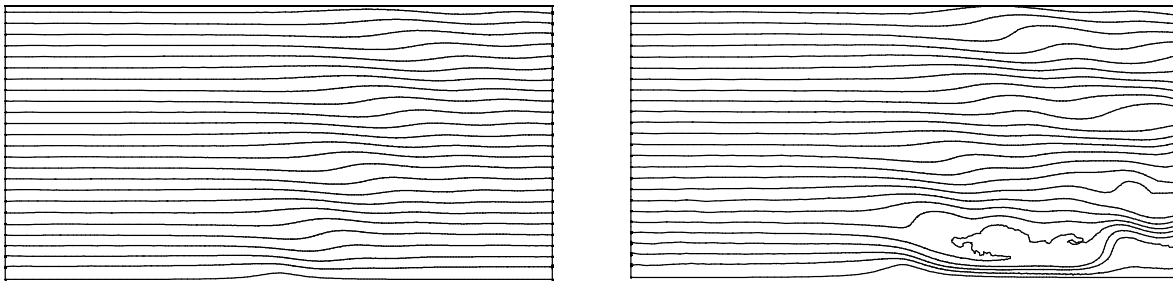
Figure 8: Isentropes simulated using the two-dimensional nonhydrostatic model; $Fr \lesssim 2$ and $Fr \lesssim 1$, in the left and right plate, respectively.

than $\approx 8\%$ in the propagation angle α. Furthermore, they both show the same distribution of the wave amplitude with height, with an average per wavelength (over seven wavelengths) loss of $\approx 7\%$ attributed primarily to the dispersive character of the nonhydrostatic mountain wave.

The canonical Boussinesq benchmark discussed above is supplemented with the simulation of the non-Boussinesq amplification and breaking of a 60km deep 2D mountain wave [34]. In contrast to the preceding example with the uniform reference profiles θ_b and ρ_b and linearly increasing constant-stratification ambient profile θ_e, here the reference profiles coincide with the ambient state and both change exponentially — such that the amplitude of the wave amplifies by one order of magnitude in the middle of the vertical extent of the model, reaching the value equal to the wavelength of the dominant mountain wave λ_0, thus inducing wave overturning and breaking. The problem is inherently nonhydro-static with $NL/U_0 \approx 1$, while only weakly nonlinear ($Fr \approx 1.6$) with respect to the linear Boussinesq theory. Figure 9 shows the model solutions using two different meshes with similar number of points. On the left the unstructured mesh mimics the structured grid (in physical space) resulting from the standard terrain-following coordinate transformation. On the right a fully unstructured triangular edge mesh is employed; cf. Fig. 5. Only mesh portions are shown in the vicinity of the hill. Both results agree with the EULAG flux-form predictions, and their departures are insignificant compared to the discrepancies
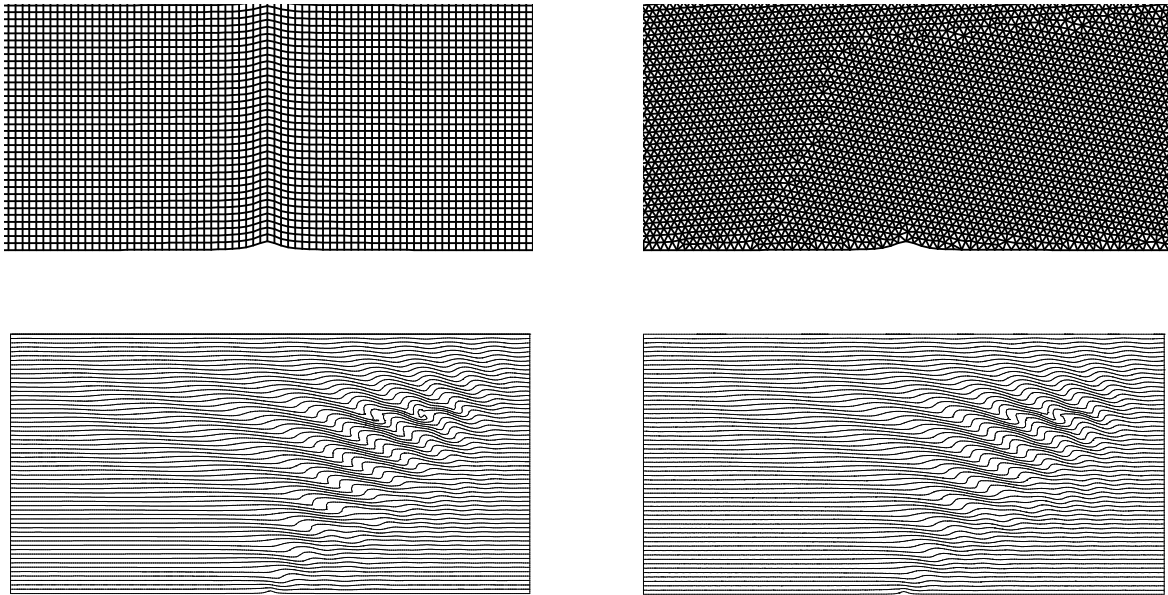
Figure 9: Meshes (top) and simulated isentropes (bottom) using the anelastic model for non-Boussinesq amplification of a mountain wave propagating in isothermal atmosphere.

between the consistent flux-form and semi-Lagrangian EULAG's solutions [34].

4.3 Towards a global unstructured mesh nonhydrostatic soundproof model

As documented in the literature and illustrated in section 3, the nonhydrostatic structured grid EULAG can be executed as a global model in the spherical geometry. The equivalent unstructured mesh variant of the code is under development, and the results of the preceding section together with those in [18, 19] already indicate that such an extension can be successful. For substantiation and illustration, here we summarize the results of [18, 19], where the wave phenomena in rotating stratified orographic flows were simulated on reduced planets [35] using isopycnic/isentropic coordinates. The calculations in [18] used isopycnic (viz. a soundproof yet mathematically elastic) framework, and kept the Earth rotation fixed while reducing the planet's radius hundredfold. Effectively this simulated a mesoscale response for different stratification regimes, from large to small Froude numbers. These calculations successfully captured characteristic flow features — from 3D wave solution at a large Froude number, to the upwind flow reversal and lee eddies formation at a low Froude number — well known from the theoretical, laboratory and numerical studies. In [19] the isentropic framework was used (viz. a compressible hydrostatic set of governing PDEs) yet the large Rossby number solutions were hardly distinguishable from the isopycnic results. Following [19], here we show the result comparing the rapidly and slowly rotating low Froude number flow past an isolated hill on the small globe.

Figure 10 shows the instantaneous distribution of the isentropes in the equatorial xz cross-section after four hours of the simulated time. Figure 11 shows the concomitant displacements of the isentropic surfaces with the undisturbed equatorial height $H(\lambda, \varphi = 0, t = 0,) = 0.25\pi U_0 N^{-1}$ (i.e., the eight of the dominant vertical wavelength λ_0 at $R_o \gg 1$) together with the flow vectors on these surfaces. Concurrently, Figs. 10 and 11 illustrate salient flow features. For the slowly-rotating, strongly-stratified case (left panels) the results evince flow blocking on the lower upwind side of the hill and intense lee eddies, characteristic of low Froude number 3D mesoscale flows [36]. For the hundredfold faster rotation
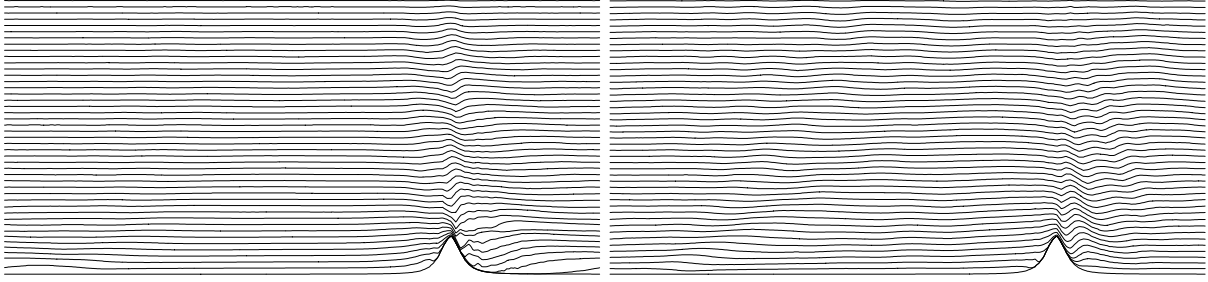
Figure 10: Isentropes in the equatorial-vertical plane, simulated using the 3D hydrostatic model for global oro-graphic flow with $Fr = 0.5$; $Ro \gg 1$ (left), and $Ro \gtrsim 1$ (right).
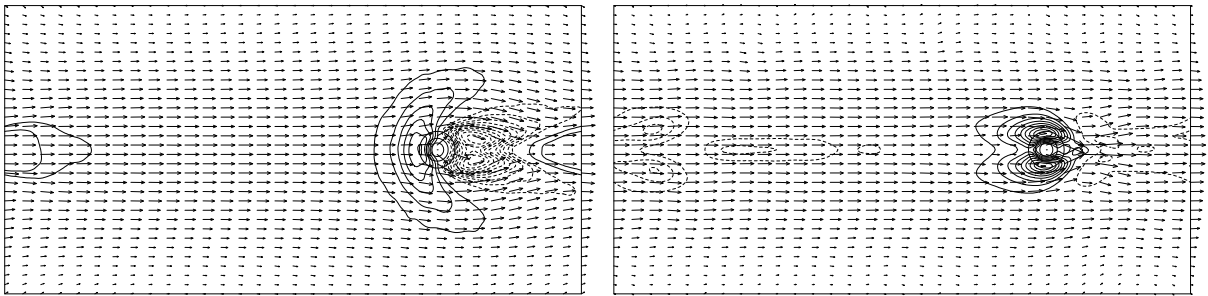

Figure 11: As in Figure 10 but for vertical displacements of, and superimposed flow vectors at, the isentropic surface with the undisturbed equatorial height $\approx 0.25\pi U_0 N^{-1}$; contours of the hill height are also superimposed.

$R_o \approx 5$,[3] the Rossby deformation radius $L_R = h_o N / f \approx 13 \cdot 10^3$ m becomes comparable to L, upon which the effects due to the rotation and stratification occur on similar horizontal scales while counteracting each other. The planetary rotation produces strong uplift of the isentropes on the mountain lateral sides and compensates the vorticity of the lee eddies, whereas aloft the mountain wave disperses with altitude. These effects are consistent with theoretical predictions [38, 36], and with the equivalent EULAG solutions (not shown) on the $128 \times 64 \times 91$ grid. Noteworthy, the unstructured mesh shown in Figure 6 (repeated at 91 isentropic levels) consists of 4532 nodes, thus effecting in about twice smaller computational problem then in EULAG. Insofar as the economy of computations is concerned, the unstructured mesh code is competitive with structured-grid program [19].

5   Remarks

There are a number of particular soundproof models used in computational meteorology. While some of them may be more restrictive than others, it has been difficult to find a numerical example reasonably relevant to NWP and climate studies conclusively showing a failure of soundproof approximations. The cumulative computational experience demonstrates surprising flexibility and a broader than anticipated range of validity of soundproof approximations. Nonhydrostatic soundproof equations imply non-negligible numerical advantages over fully compressible equations, and the developments of the last decade document growing interest of the community in exploiting their strengths.

---

[3]Because $f = 0$ at the equator but the results depend on the rotation rate, $f = 2\Omega \sin(L/a)$ is used as a more representative value; cf. section 4 in [37] for a discussion.

An increased activity and rapid progress in modeling atmospheric flows on unstructured/hybrid meshes with flexible adaptivity have already provided evidence of the potential and merits of finite-volume discretizations for modeling all-scale atmospheric circulations. In particular, results emerge indicating the competitiveness of the unstructured-mesh models in terms of accuracy and computational efficiency. Even though unstructured-mesh models are not yet (and may never be) poised to substitute for the operational weather and climate codes traditionally formulated on structured grids, it is quite conceivable that future Earth System models will blend unstructured meshes and structured grids for the benefit of forecast and research.

Acknowledgements

References

[1] Special Issue 'Predicting weather, climate and extreme events' Guest Editors M.J. Miller and P.K. Smolarkiewicz, *J. Comput. Phys.* 2008, **227**:3429-3730.

[2] Davies T, Staniforth A, Wood N, Thuburn J. Validity of anelastic ond other equation sets as inferred from normal-mode analysis. *Q.J.R. Meteorol. Soc.* 2003, **129**:2761-2775.

[3] Ogura Y, Phillips NA, Scale analysis of deep and shallow convection in the atmosphere. *J. Atmos. Sci.* 1962, **19**:173-179.

[4] Lipps FB, Hemler RS. A scale analysis of deep moist convection and some related numerical calculations. *J. Atmos. Sci.* 1982, **39**:2192-2210.

[5] Prusa JM, Smolarkiewicz PK. An all-scale anelastic model for geophysical flows: dynamic grid deformation. *J. Comput. Phys.* 2003, **190**:601-622.

[6] Wedi NP, Smolarkiewicz PK. Extending Gal-Chen & Somerville terrain-following coordinate transformation on time-dependent curvilinear boundaries. *J. Comput. Phys.* 2004, **193**:1-20.

[7] Smolarkiewicz PK, Prusa JM, Toward mesh adaptivity for geophysical turbulence: continuous mapping approach. *Int. J. Numer. Meth. Fluids* 2005, **47**:789-801.

[8] Durran DR. A physically motivated approach for filtering acoustic waves from the equations governing compressible stratified flow. *J. Fluid Mech.* 2008, **601**:365-379.

[9] Durran DR. Improving the anelastic approximation. *J. Atmos. Sci.* 1989, **46**:1453-1461.

[10] Abiodun BJ, Prusa JM, Gutowski WJ Jr. Implementation of a non-hydrostatic, adaptive-grid dynamics core in CAM3. Part I: comparison of dynamics cores in aqua-planet simulations, *Clim. Dyn.* 2008, **31**:795-810.

[11] Abiodun BJ, Gutowski WJ Jr, Prusa JM. Implementation of a non-hydrostatic, adaptive-grid dynamics core in CAM3. Part II: dynamical influences on ITCZ behavior and tropical precipitation, *Clim. Dyn.* 2008, **31**:811-822.

[12] Neale RB, Hoskins BJ, A standard test for AGCMs including their physical parameterizations, I: the proposal, *Atmos. Sci. Lett* 2000, doi:10.1006/asle.2000.0019

[13] Neale RB, Hoskins BJ, A standard test for AGCMs including their physical parameterizations, II: results for the Met Office Model, *Atmos. Sci. Lett* 2000, doi:10.1006/asle.2000.0020

[14] Prusa JM, Smolarkiewicz PK, Wyszogrodzki AA, EULAG, a computational model for multiscale flows, *Comput. Fluids* 2008, **37**:1193-1207.

[15] Arakawa A, Konor C, Unification of the anelastic and quasi-hydrostatic systems of equations, *Month. Weather Rev.* 2009, **137**:710-726.

[16] Klein R, Achatz U, Bresch D, Knio OM, Smolarkiewicz PK, Regime of validity of soundproof atmospheric flow models, *J. Atmos. Sci.* 2010, **67**:3226-3237.

[17] Smolarkiewicz PK, Szmelter J, Iterated upwind schemes for gas dynamics, *J. Comput. Phys.* 2009, **228**:33-54.

[18] Szmelter J, Smolarkiewicz PK, An edge-based unstructured mesh discretisation in geospherical framework, *J. Comput. Phys.* 2010, **229**:4980-4995

[19] Szmelter J, Smolarkiewicz PK, An edge-based unstructured mesh framework for atmospheric flows, *Comput. Fluids* 2010, in press.

[20] Prusa JM, Gutowski WJ, Multi-scale features of baroclinic waves in soundproof, global simulations with EULAG, *Proc. V European Conference on Computational Fluid Dynamics*, Lisbon, Portugal, 2010, ECCOMAS paper #1453, 18 pp.

[21] Jablonowski C, Williamson DL, A baroclinic instability test case for atmospheric model dynamical cores, *Q.J.R. Meteorol. Soc.* 2006, **132**:2943-2975.

[22] Grabowski WW, Smolarkiewicz PK. A multiscale anelastic model for meteorological research, *Mon. Weather Rev.* 2002, **130**:939-956.

[23] Smolarkiewicz PK, Winter CL, Pores resolving simulation of Darcy flows. *J. Comput. Phys.* 2010, **229**:3121-3133

[24] Ghizaru M, Charbonneau P, Smolarkiewicz PK, Magnetic cycles in global large-eddy simulations of solar convection, *Astrophys. J. Lett.* 2010, **715**:L133-L137.

[25] Smolarkiewicz PK, Dörnbrack A, Conservative integrals of adiabatic Durran's equations. *Int. J. Numer. Meth. Fluids* 2008, **56**:1513-1519.

[26] Smolarkiewicz PK, Multidimensional positive definite advection transport algorithm: an overview, *Int. J. Numer. Meth. Fluids* 2006, **50**:1123-1144.

[27] Smolarkiewicz PK, Szmelter J, MPDATA: An edge-based unstructured-grid formulation, *J. Comput. Phys.* 2005, **206**:624-649.

[28] Program of The 2010 Workshop on the Solution of PDEs on the Sphere; http://www.awi-potsdam.de/pde2010/pdes2010#Program

[29] Williamson DL, The evolution of dynamical cores for global atmospheric models, *J. Meteor. Soc. Japan* 2008, **85B**:241-268.

[30] Theme Issue 'Mesh generation and mesh adaptation for large-scale Earth-system modelling' compiled and edited by N. Nikiforakis, *Phil. Trans. R. Soc. A* 2009, **367**:4473-4654.

[31] Barth TJ. Aspects of unstructured grids and finite volume solvers for the Euler and Navier-Stokes equations. In *Special Course on Unstructured Grid Methods for Advection Dominated Flows* 1992, AGARD Report 787:6.1–6.61.

[32] P.K. Smolarkiewicz, C. Temperton, S.J. Thomas, and A.A. Wyszogrodzki. Spectral Preconditioners for nonhydrostatic atmospheric models: extreme applications. *Proceedings of the ECMWF Seminar Series on Recent developments in numerical methods for atmospheric and ocean modelling*, Reading, UK, 2004, 203-220.

[33] Dutton J.A. The Ceaseless Wind. Dover Publications, 1986, pp. 617.

[34] Smolarkiewicz PK, Margolin LG. On forward-in-time differencing for fluids: An Eulerian/semi-Lagrangian nonhydrostatic model for stratified flows. *Atmos. Ocean Special* 1997, **35**:127-152.

[35] N.P. Wedi and P.K. Smolarkiewicz, A Framework for testing global nonhydrostatic models, *Q.J.R. Meteorol. Soc.* 2009, **135**:469–484.

[36] J.C.R. Hunt, H. Olafsson and P. Bougeault, Coriolis effects on orographic and mesoscale flows, *Q.J.R. Meteorol. Soc.* 2001, **127**:601-633.

[37] Kuettner J., Easterly flow over the cross equatorial island of Sumatra and its role in the formation of cyclone pairs over the Indian ocean, *Weter und Leben* 1989, **41**:47-55.

[38] R.B. Smith, The influence of the mountains on the atmosphere, *Advances in Geophysics* 1979, **21**:87–230.